High-frequency *Po/So* guided waves in the oceanic lithosphere: I—long-distance propagation

B. L. N. Kennett[1] and T. Furumura[2]

[1]*Research School of Earth Sciences, The Australian National University, Canberra ACT* 0200, *Australia. E-mail: Brian.Kennett@anu.edu.au*
[2]*Earthquake Research Institute, The University of Tokyo,* 1-1-1 *Yayoi, Bunkyo-ku, Tokyo,* 113-0032, *Japan*

SUMMARY

In many parts of the ocean high-frequency seismic energy is carried to very great distances from the source. The onsets of the *P* and *S* energy travel with speeds characteristic of the mantle lithosphere. The complex and elongated waveforms of such *Po* and *So* waves and their efficient transport of high frequencies (>10 Hz) have proved difficult to explain in full. Much of the character can be captured with stratified models, provided a full allowance is made for reverberations in the ocean and the basal sediments. The nature of the observations implies a strong scattering environment. By analysing the nature of the long-distance propagation we are able to identify the critical role played by shallow reverberations in the water and sediments, and the way that these link with propagation in a heterogeneous mantle. 2-D finite difference modelling to 10 Hz for ranges over 1000 km demonstrates the way in which heterogeneity shapes the wavefield, and the way in which the properties of the lithosphere and asthenosphere control the nature of the propagation processes. The nature of the *Po* and *So* phases are consistent with pervasive heterogeneity in the oceanic lithosphere with a horizontal correlation length (∼10 km) much larger than the vertical correlation length (∼0.5 km).

Key words: Body waves; Guided waves; Computational seismology; Wave scattering and diffraction; Wave propagation.

1 INTRODUCTION

Oceanic *Pn* and *Sn* (often referred to as *Po* and *So*) are high-frequency arrivals with long coda that travel for large distances across the deep ocean basins. These phases have been observed after propagation for more than 3000 km in the Pacific (Walker & Sutton 1971). The *Po* arrival with an apparent velocity around 8.1 km s^{-1} normally contains significant contributions from frequencies above 15 Hz. The *Po* wave train is commonly longer than the *So* wave train, but the frequency content of *So* is comparable, or higher, than *Po* (Walker *et al.* 1983). The onsets of *Po* and *So* tend to be emergent with a gradual build up of energy reaching a maximum at an apparent velocity close to that for the base of the crust. The onset of *P* is normally lower frequency than *Po*, which follows after a short interval with much higher frequency content that decays only slowly. A similar effect for *So* is frequently obscured by the continuing coda of *Po*.

A range of examples of waveforms of *Po* and *So* on hydrophones and ocean-bottom seismometers are presented by Brandsdóttir & Menke (1988). These examples illustrate the way in which the instrumental responses interact with the propagation effects to shape the apparent character of the arrivals.

Fig. 1 illustrates the typical complex shape of *Po* and *So* arrivals for ocean bottom seismometer (OBS) recordings from the Northwestern Pacific. We display a record section for a set of similar, shallow events along the Pacific Plate margin from Izu-Bonin to the northern end of the Kurile arc, organized in terms of epicentral distance (the event parameters are presented in Table 1). These records were obtained by broad-band ocean bottom sensors (Shiobara *et al.* 2005) developed and operated by the Ocean Hemisphere Project Data Management Center (OHPDMC) at the Earthquake Research Institute, the University of Tokyo. We have applied an instrumental response correction and a band pass filter with a pass band between 1 and 10 Hz, to emphasize the *Po* and *So* phases and to allow comparison with numerical simulations presented later in the paper. The seismic records represent radial (R) component velocity motion. The traces are aligned at the arrival of the initial *P* phase and the amplitude is normalized by the *S* wave. All events at NWPAC1-3 display well developed *Po* and *So* wave trains with high frequency content and very long coda, but there are notable differences in the relative proportions of *Po* and *So* between events. The complex character of *Po* and *So* with high frequency content and long coda is independent of the nature of the focal mechanism.

The records in Fig. 1 have been selected to emphasize the component of propagation in the oceanic lithosphere. In contrast, Shito *et al.* (2013) have illustrated *Po* and *So* results from deeper events (>100 km depth) beneath and behind the Japanese islands, where

GJI Seismology
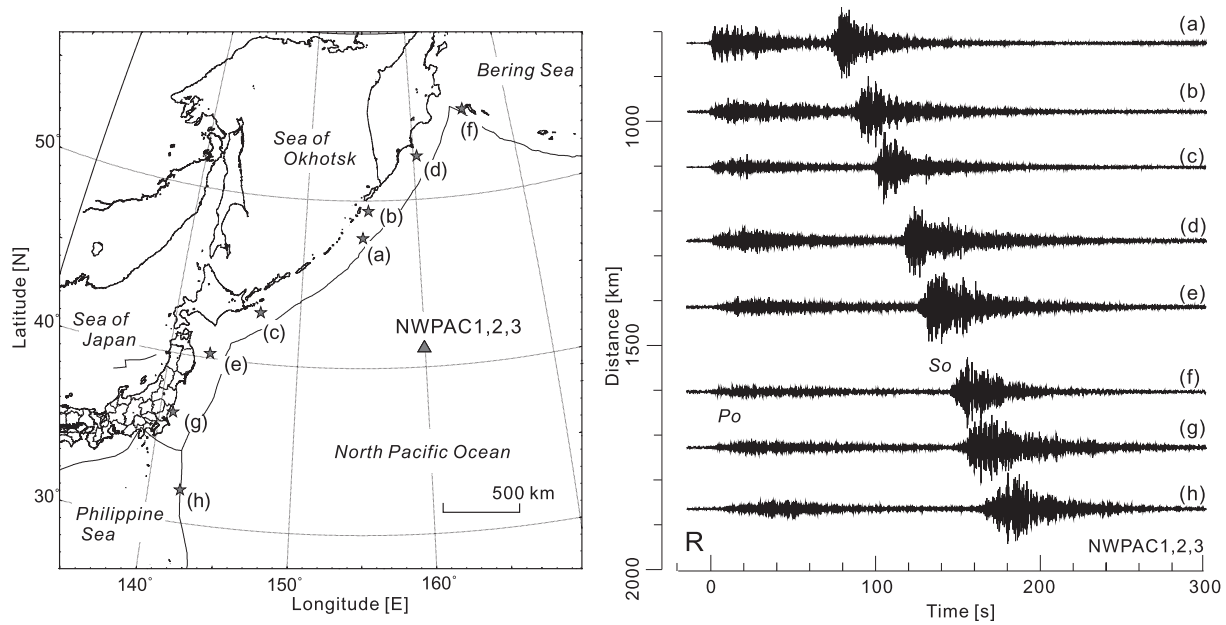
Figure 1. Record section of OBS records for *Po*, *So*; left-hand panel: map of events, right-hand panel: radial component records at stations NWPAC1, 2 and 3 (Stations 1–3 are in same location but operated at different times).

Table 1. Event parameters for Figs 1 and 2.

| ID	yyyy/mm/dd	hh:mm:ss.s	Lat. (N)	Lon. (E)	Dep. (km)	Mag.	Dist. (km)
(a)	2001/10/09	23:53:37.0	47.758	155.102	33	5.9	830.6
(b)	2002/01/28	13:50:28.7	49.381	155.594	33	6.1	977.9
(c)	2000/08/15	20:20:43.8	43.046	146.759	33	5.8	1110.0
(d)	2001/10/08	18:14:26.4	52.591	160.324	48	6.5	1274.5
(e)	2000/10/03	04:13:30.4	40.282	143.124	33	6.3	1421.6
(f)	1999/11/26	00:29:00.2	55.133	165.364	33	6.0	1608.7
(g)	2000/07/20	18:39:18.8	36.510	140.983	47	6.0	1719.6
(h)	1999/10/25	07:29:55.5	31.971	142.251	33	5.8	1875.0
(A)	1999/10/24	04:21:39	44.578N	149.443E	41	5.7	1110.0
(B)	2000/06/15	11:10:46	29.332N	132.097E	11	6.0	1150.9

the time separation between the low frequency onset of *P* and the slightly later arrival of high-frequency *Po* is more pronounced. The lower-frequency direct arrivals from the deeper events travel through the asthenosphere with a distinct path difference from the high-frequency guided *Po* in the lithosphere.

The study by Brandsdóttir & Menke (1988) indicates that *So* is more variable in character than *Po*, most likely because the shorter wavelengths make it more susceptible to the influence of structure along the propagation path. We illustrate such variations in Fig. 2 with three-component OBS records for two events at a similar epicentral distance at stations on the Pacific and Philippine Sea Plate. The lithosphere of the Philippine Sea Plate is younger and thinner than that for the Pacific Plate, and the relative amplitude of *So* to *Po* is much reduced at PHS08 compared with NWPAC1.

The three component records in Fig. 2 are rotated so that the radial component (R) lies along the great-circle to the source, yet the perpendicular component (T) transverse to the path shows a very significant component of *P*-wave energy at both stations. The relatively modest level of excitation on the vertical component is associated with the near horizontal propagation of both *P* and *S* waves.

In a stratified medium there would be no contribution to the transverse component until the arrival of *S*. The strong high frequency content in the *Po* and *So* arrivals, and the off great-circle propagation to produce strong *Po* on the T component is indicative of intense scattering in the passage of the seismic wave energy from source to receiver.

In Fig. 3, we summarize results for *Po*, *So* in the northwest Pacific region, combining the events tabulated by Brandsdóttir & Menke (1988), those used by Shito *et al.* (2013), and those we have analysed directly. Propagation in the Pacific Plate is most efficient to ocean bottom instruments, shown in Fig. 3 by solid symbols. At island stations (open symbols in Fig. 3) the noise levels are generally larger and there is a complex interaction between the guided waves and the island itself. *Po* and *So* are observed from events at a wide range of depths in the subduction zones as well as outer rise events. There is a strong contrast between the generally efficient propagation of *So* in the Pacific Plate and the very variable properties for paths crossing the Philippine Sea Plate. The Philippine Sea Plate is younger and more heterogeneous in lithosphere thickness. It is rare to get strong *So* propagation for more than a few hundred kilometres. Paths from the same event show very different character depending on whether
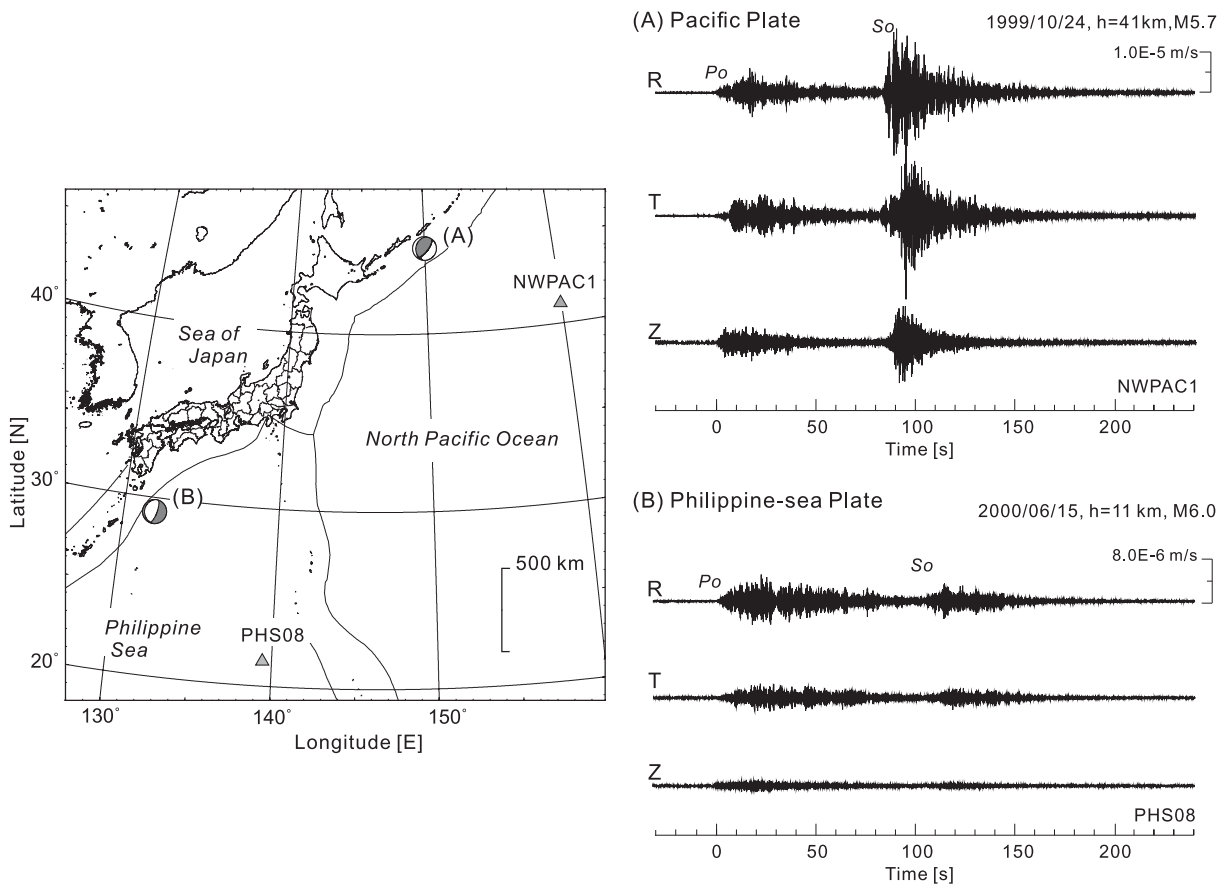
Figure 2. Comparison of three-component OBS records for *Po*, *So* for events at similar distances recorded on (a) Pacific Plate and (b) Philippine Sea Plate. The events are normalized by the *Po* amplitude.

the paths traverse the old lithosphere of the Pacific Plate or the younger Philippine Sea Plate.

2 NATURE OF *Po* AND *So*

Modelling by Sereno & Orcutt (1985) using a wavenumber integration code for a layered structure demonstrated the importance of multiple reverberations in the water column and sediments in controlling the character of long-distance propagation of seismic waves across the ocean. Sereno & Orcutt (1987) used an improved representation of the crust and upper mantle to model *Po* and *So* data collected from the 1983 Ngendei Seismic Experiment in the southwestern Pacific; their work showed the importance of water-sediment reverberation in shaping the *Po/So* spectra. Sereno & Orcutt (1987) were also able to obtain relatively long *Po* coda in a laterally homogeneous model without any fine-scale structure in the lithosphere and the mantle beneath.

Mallick & Frazer (1990) introduced more complex models with up to 2 per cent random velocity perturbations in the 1-D profile through the crust and mantle, and were thereby able to get a closer match to the features of *Po/So* at a subbottom seismometer (OSSIV) in the northwest Pacific for earthquakes in the Kurile trench. The vertically varying random fluctuations can be regarded as simulating large-aspect-ratio lenticular structures as envisaged by Fuchs & Schulz (1976). The reflectivity modelling used by Mallick & Frazer (1990) utilized parallel computation procedures to secure high frequency calculations at large distances, but was still restricted to laterally uniform models.
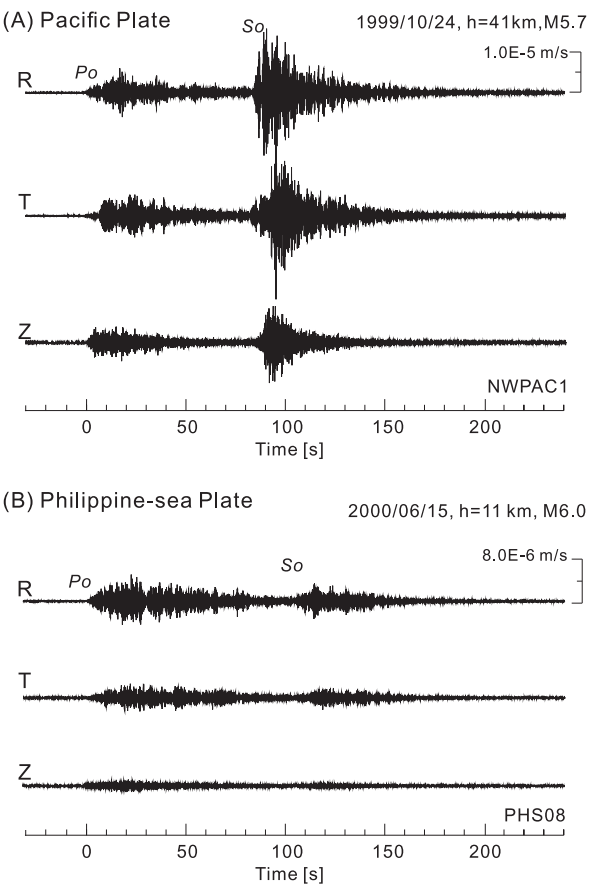
With the progressive increase in computation power it has become possible to undertake very high frequency calculations for complex 2-D structures, in particular the investigations of high-frequency guided waves in subduction zones (Furumura & Kennett 2005, 2008; Shito *et al.* 2013) and the continental lithosphere (Kennett & Furumura 2008). Shito *et al.* (2013) demonstrate the importance of a quasi-lamina structure with horizontally elongated scatterers in the lithosphere to develop high-frequency and long-duration *P* and *S*-wave coda from deep-focus earthquakes.

We here use such finite difference calculations for investigating the influence of lateral heterogeneity on long-range guiding of high-frequencies in the oceanic lithosphere to distances of 1100 km, for frequencies up to 10 Hz. We examine the way in which different classes of heterogeneity in the oceanic lithosphere modify the wavefield and contribute to the nature of the coda.

We confirm the importance of the water and sediment reverberations noted by Sereno & Orcutt (1985, 1987), but now we are able to carry the calculations into a situation with variable lateral heterogeneity superimposed on a smooth background crustal and upper mantle model. The reverberations play a major role in extending the coda of *Po* and *So*, but are modified by the interaction with heterogeneity to smear out any distinct arrivals.

Insight into the character of the propagation process can be obtained by using a representation in terms of reflection and transmission operators for laterally varying media (*cf.* Kennett 1986). We are able to demonstrate how the water-sediment reverberations determine the main character of the wavefield, and by extracting a background stratified structure gain insight into the
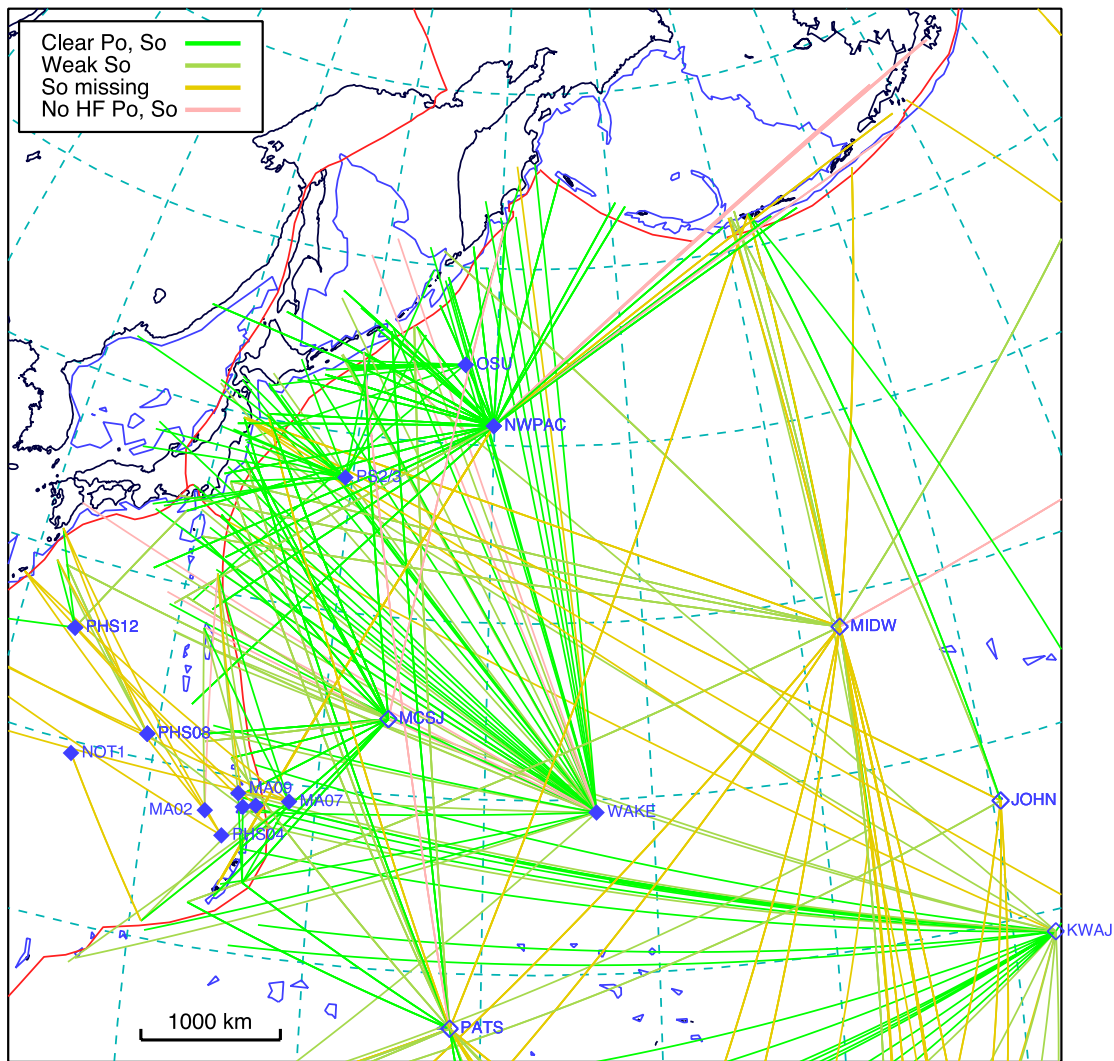
Figure 3. Propagation characteristics for *Po* and *So* phases in the northwest Pacific region. Solid symbols indicate ocean bottom instruments, and open symbols island stations. Efficient propagation of both *Po* and *So* occurs across a broad region. *So* tends to be less noticeable for very long paths and where paths cross island chains.

nature of scattering that is useful in understanding the numerical results.

3 LONG RANGE PROPAGATION IN THE OCEANIC LITHOSPHERE

We illustrate the way in which high-frequency waves are guided in the oceanic lithosphere using simulations of seismic wave propagation in heterogeneous structures with a 2-D finite difference method (FDM). We have started from the stratified model used by Sereno & Orcutt (1987) and superimposed various styles of stochastic lateral heterogeneity in the crust and mantle. The 2-D model used for the simulation covers a region of 1200 km horizontally and 168 km in depth, discretized with a uniform grid interval of 0.04 km in both directions. Earth flattening is applied to the model of *P* and *S* wave speed (V_p, V_s) in order to include the effect of the sphericity of the Earth in a cartesian-coordinate system, so that the model can be used with conventional rectangular FDM grid.

A double-couple line source (dip 45°) has been placed at a depth of 33 km. The high-frequency seismic wavefield (above 1 Hz) is not very sensitive to the details of the source mechanism, because multiple scattering of seismic waves in the heterogeneous crust- and upper-mantle structure disrupts the radiation patterns rather strongly (e.g. Takemura *et al.* 2009). The seismic source-slip function is a pseudo-delta function which radiates seismic waves with a maximum frequency of 10 Hz.

To achieve long distance propagation at high frequencies (10 Hz) a parallel implementation of the FDM is employed in a staggered-grid configuration with 4th-order accuracy in space and 2nd-order accuracy in time (Furumura & Chen 2004). The simulation is conducted by using 16 nodes (64 CPUs) of the Earth Simulator supercomputer at the Japan Agency for Marine-Earth Science and Technology. Frequency independent anelastic attenuation for *P* and *S* waves (Q_p, Q_s) is introduced into the FDM simulation using the memory variable technique of Hestholm (1999). We employed a broad-band Q model using three memory variables and a reference frequency $f_0 = 0.5$ Hz. This yields constant Q_p and Q_s in a wide frequency band below f_0, and Q_p and Q_s increase gradually with increasing frequency above f_0.

Because our simulation evaluates a complex seismic wavefield with multiple reverberations of seismic waves in the water column sandwiched by air and solid, we applied the proper boundary

conditions at the free surface air/liquid interface (Okamoto & Takenaka 2005). At the sea bottom we employed a representation of the fluid/solid interface using a 2nd-order FDM to achieve zero-tangential-stress conditions (for detail see Maeda & Furumura 2013) rather than the 4th-order staggered-grid scheme used through the rest of the model.

We also applied an effective absorbing boundary conditions to surpress artificial reflections from the bounded domain by employing a perfect matching layer (PML) technique using the procedure of Marcinkovich & Olsen (2003) and Moczo *et al.* (2007). The PML boundary condition is applied in a 10-gridpoint zone surrounding the model.

The simulations are carried out in 2-D, whereas the environment in the oceanic lithosphere clearly manifests 3-D heterogeneity, as can be seen from the *P*-wave energy appearing on the transverse component observed seismograms in Fig. 2. Kennett & Furumura (2008, appendix) have undertaken a set of comparative tests for 2-D, 2.5 D and 3-D models and have demonstrated that the class of 2-D model used in this study is well suited to describe the main characteristics of the scattering wavefield in 3-D, even though out-of-plane scattering is excluded. The weaker geometrical spreading in 2-D tends to compensate for this effect. In 2-D we can carry out simulations to high frequencies over long distances, whereas any 3-D calculations would necessarily be much more restricted.

There is considerable variation in the relative amplitudes of observed *Po* and *So* for observed seismograms, in part from the variation on source mechanism, but also reflecting the propagation environment. The properties of some observations have been modelled with Q_s roughly twice Q_p, with both increasing with frequency (Mallick & Fraser 1990). Such behaviour is difficult to reconcile with the normal situation with very little loss in bulk compression for which $Q_p/Q_s \approx 2.2$ (e.g. Jackson 2007). In the set of calculations below we have assumed a rather conservative model for attenuation with little frequency dependence, and as a result our results may tend to underestimate the the likely *So* arrival. Thus the relative amplitude of *So* to *Po* is not as large as that in Fig. 2 for the Pacific Plate, but larger than that for the Philippine Sea Plate.

We have undertaken a broad range of numerical simulations with the aim of finding classes of lithospheric structure that are compatible with the nature of observations of *Po* and *So* after propagation for several hundred kilometres. We will here present a sequence of models of increasing complexity to demonstrate the way in which presence of heterogeneity builds up the complex coda for *Po* and *So*. For each class of structure we present a record section of computed radial (R) component seismograms from 200 to 1100 km from the source using a reduction velocity of 8.5 km s^{-1}, and also exploit snapshots of selected aspects of the wavefield.

We first illustrate the role of lateral heterogeneity superimposed on a base structure (Fig. 4) derived from the work of Sereno & Orcutt (1987). This structure is covered by a 4-km-thick water ($V_p = 1.5$ km s^{-1}, $Q_p = 50\,000$) and 0.5-km-thick low-wave speed and high attenuative sediment ($V_p = 2.0$ km s^{-1}, $V_s = 1.154$ km s^{-1}; $Q_p = 200$, $Q_s = 100$).

For the stratified base model (Fig. 5a), we obtain elongated wave trains particularly for *P* with a groups of distinct arrivals associated with multiple reverberations in the water column and sediments, as can be seen clearly in the snapshot at 72 s after source initiation (Fig. 5b). The separation of the *P* and *S* components of the wavefield in the snapshots is obtained by calculating the divergence and curl of the 2-D wavefield. The water reverberations impose a strong banding on the sequence of wave fronts for both *P* and *S*. In the
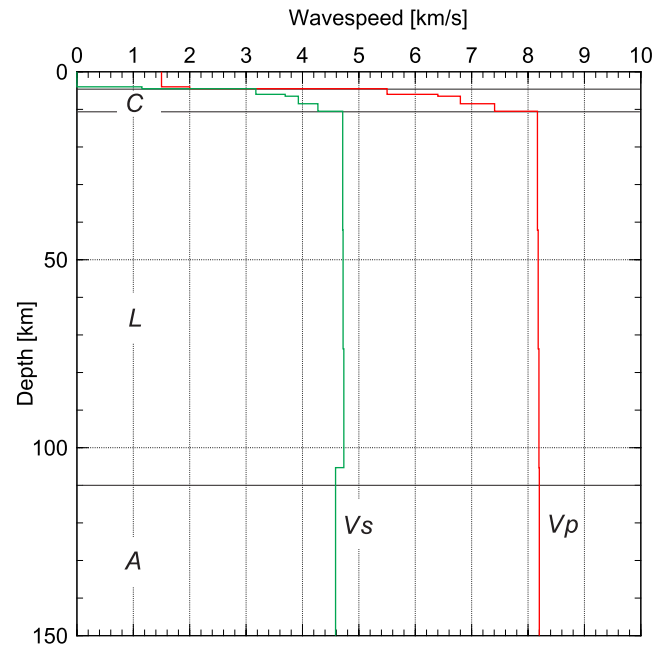
Figure 4. Background wave speed model for *P* and *S* derived from the work of Sereno & Orcutt (1987), used in combination with different heterogeneity structures in the crust (C), lithosphere (L), and asthenosphere (A). See Table 2.

lithosphere there is a weak velocity gradient and so multiple reflections beneath the crust–mantle interface will set up a 'whispering gallery effect' (Menke & Richards 1980) that will be truncated once a component of the wavefield penetrates into the asthenosphere and seismic energy escapes from the lithosphere into the lower velocity material below. Each of the water reverberations will link into such a sequence contributing to the complexity of the waveforms. The waveforms in Fig. 5 confirm the reflectivity calculations undertaken by Sereno & Orcutt (1987) as to the importance of the water and sediment reverberations. As we see such water and sedimentary reverberations continue to play an important role when the properties of the oceanic lithosphere vary horizontally as well as in depth.

### 3.1 Nature of propagation processes

We are able to gain an understanding of the nature of the influences on long-range seismic wave propagation in the ocean by using the reflection and transmission properties of the components of the structure (e.g. Kennett 2001). Kennett (1984) has shown that there is a direct correspondence between the results obtained using matrix methods in the frequency-slowness domain for a stratified medium and more general structures provided that the matrices are reinterpreted as operators.

Consider then a model with a water and sediment layer overlying oceanic crust and mantle (Fig. 6) with a source at the level z_S generating both upgoing and downgoing waves. We introduce the water surface *f*, the water bottom at *w* and the base of the sediments at *b* and develop an operational representation for the seismic response at an ocean-bottom seismometer sitting just below the seafloor.

In the most direct representation we construct the upgoing field at the source level as the sum of the upgoing radiation from the source U_S and the contribution from downgoing radiation reflected
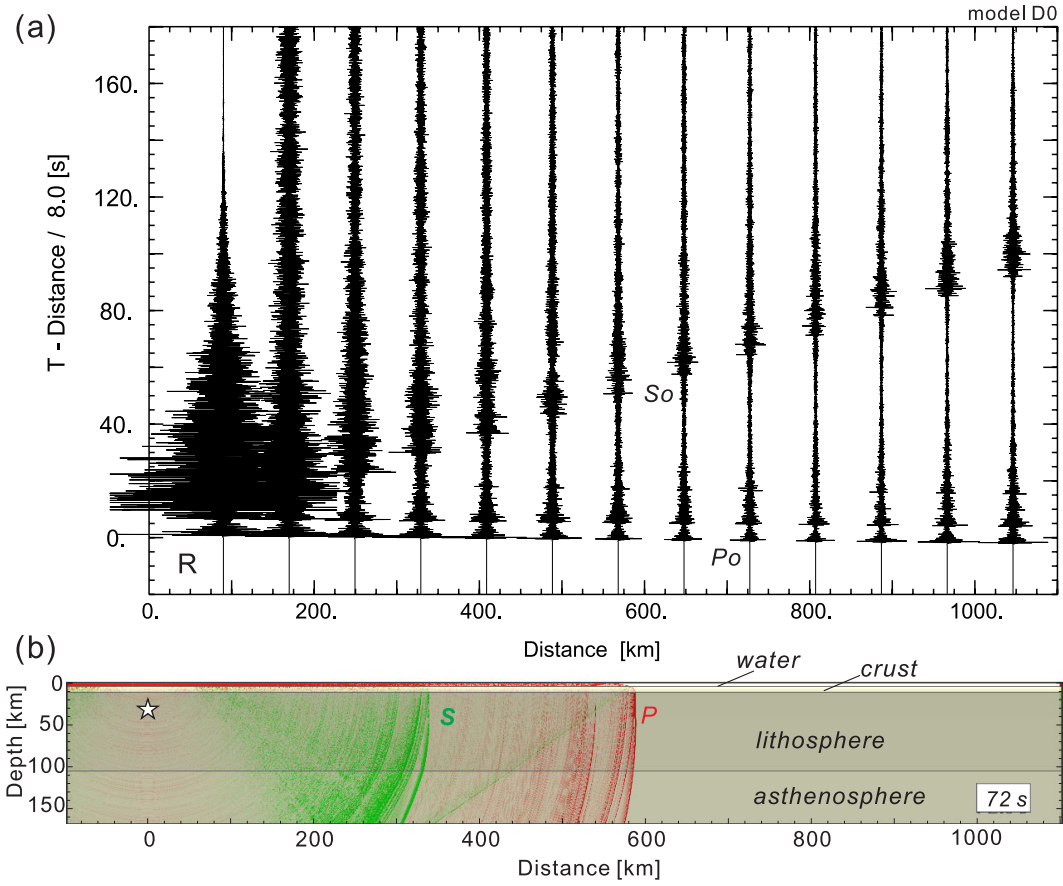
Figure 5. (a) Record section of radial component seismograms for the base stratified model shown in Fig. 4, the water and sediment reverberations lead to distinct pulses in the *P* and *S* arrivals; (b) Snapshot of wavefield at 72 s after source initiation: *P*-wave energy is shown in red and *S*-wave energy in green. The water reverberations impart a strongly banded structure on the wave fronts.
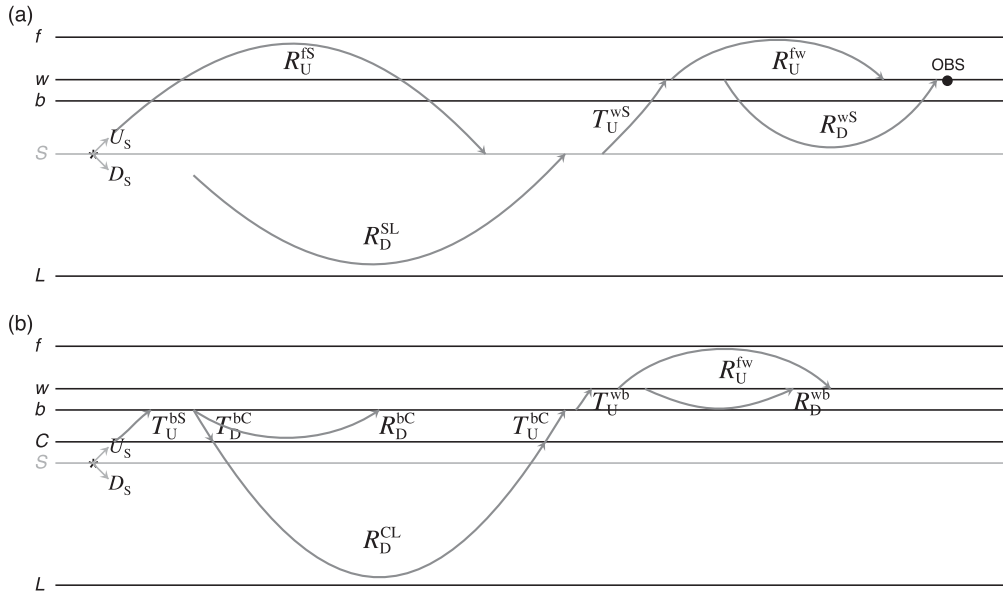
Figure 6. Representation of the propagation elements involved in long-distance propagation through the oceanic lithosphere: (a) direct representation (b) additional components of importance when a split in the structure is made at the base of the sediments.

back from the structure beneath the source level $R_D^{SL} D_S$. Both parts are modulated by reverberation in the full structure so that

$$v_U(z_S) = \left[I - R_D^{SL} R_U^{fS}\right]^{-1} \left[U_S + R_D^{SL} D_S\right], \tag{1}$$

where R_U^{fS} represents the operational effect of reflection from all the structure lying above the source level. The reverberation operator $[I - R_D^{SL} R_U^{fS}]^{-1}$ is to be interpreted as representing the cumulative effect of all the multiple reflections above and below the

source level: $I + R_D^{SL} R_U^{fS} + R_D^{SL} R_U^{fS} R_D^{SL} R_U^{fS} + \cdots$. When we include transmission to the seabed from the source level and allowance for the interaction of upgoing and downgoing waves we obtain the displacement at the ocean-bottom seismometer in the form

$$w_{\mathrm{OBS}} = \left\{ W_U^w + W_D^w R_U^{fw} \right\} \left[I - R_D^{wS} R_U^{fw} \right]^{-1} T_U^{wS} v_U(z_S),$$

$$= \left\{ W_U^w + W_D^w R_U^{fw} \right\} \left[I - R_D^{wS} R_U^{fw} \right]^{-1} T_U^{wS} \left[I - R_D^{SL} R_U^{fS} \right]^{-1}$$

$$\times \left[U_S + R_D^{SL} D_S \right], \tag{2}$$

where W_U^w, W_D^w represent the displacement operators for upgoing and downgoing waves at the water bottom. The reflection operator R_U^{fw} is dominated by the reflection from the water surface and the operators R_D^{wS}, T_U^{wS} include the reflection and transmission effects of the zone between the source and the seafloor. The reverberatory effects of the water column and sedimentary layers are included through the influence of the free-surface reflection operators R_U^{fS}, R_U^{fw} in $[I - R_D^{wS} R_U^{fw}]^{-1}$, and $[I - R_D^{SL} R_U^{fS}]^{-1}$.

In the water we have only P-wave propagation, and reflection from the sea surface is very efficient so that there is little loss in multiple free surface interactions. The diagonal components of the operator matrices represent propagation in a single wavetype. In long distance propagation the significant contributions come from near grazing incidence, at large angles from the vertical, and so there is strong seismic energy return in operators such as R_D^{wS}, R_D^{SL}. This means that the reverberation operators $[I - R_D^{wS} R_U^{fw}]^{-1}$, and $[I - R_D^{SL} R_U^{fS}]^{-1}$ dominate the response.

To concentrate on the specific influence of the water and sedimentary layers we make use of the device of an effective source at the level b (just below the base of the sediments). The equivalent radiation terms at b corresponding to the true source at the level Z_S are

$$U_b = T_U^{bS} U_S - R_D^{bS} \left(T_D^{bS} \right)^{-1} \left[R_U^{bS} U_S + D_S \right], \tag{3}$$

$$D_b = \left(T_D^{bS} \right)^{-1} \left[R_U^{bS} U_S + D_S \right], \tag{4}$$

where we have used the operator generalizations of the results of Kennett (1983, chapter 9). Further the reflection operator for the zone below b is

$$R_D^{bL} = R_D^{bS} + T_U^{bS} \left[I - R_D^{SL} R_U^{bS} \right]^{-1} R_D^{SL} T_D^{bS}. \tag{5}$$

Thus if we now construct the net apparent upgoing radiation at b we have

$$\left[U_b + R_D^{bL} D_b \right] = T_U^{bS} U_S + T_U^{bS} \left[I - R_D^{SL} R_U^{bS} \right]^{-1}$$

$$\times R_D^{SL} \left[D_S + R_U^{bS} U_S \right], \tag{6}$$

which consists entirely of physically realizable processes and has no dependence on $(T_D^{bS})^{-1}$. The full upgoing field at b has the analogous form to (1):

$$v_U^b = \left[I - R_D^{bL} R_U^{fb} \right]^{-1} \left[U_b + R_D^{bL} D_b \right], \tag{7}$$

and the response at the ocean-bottom seismometers can now be expressed as

$$w_{\mathrm{OBS}} = \left\{ W_U^w + W_D^w R_U^{fw} \right\} \left[I - R_D^{wb} R_U^{fw} \right]^{-1} T_U^{wb} v_U^b,$$

$$= \left\{ W_U^w + W_D^w R_U^{fw} \right\} \left[I - R_D^{wb} R_U^{fw} \right]^{-1} T_U^{wb} \left[I - R_D^{bL} R_U^{fb} \right]^{-1}$$

$$\times \left[U_b + R_D^{bL} D_b \right]. \tag{8}$$

In the representation described by (6)–(8) the influence of water and sediments are now confined to R_U^{fb} and occur explicitly in the reverberation operator $[I - R_D^{wb} R_U^{fw}]^{-1}$. We can expand the reflection operator for the region above b so that the same water and sediment reverberation term is extracted:

$$R_U^{fb} = R_U^{wb} + T_D^{wb} R_U^{fw} \left[I - R_D^{wb} R_U^{fw} \right]^{-1} T_U^{wb} = R_U^{wb} + Z^{fwb}. \tag{9}$$

In the main reverberation operator appearing in (7)

$$\left[I - R_D^{bL} R_U^{fb} \right]^{-1} = \left[I - R_D^{bL} \left(R_U^{wb} + Z^{fwb} \right) \right]^{-1}. \tag{10}$$

Further isolation of the water effects can be achieved by using an expansion of the reverberation operator as described in the Appendix (eq. A.8). If we identify the operator A with $R_D^{bL} R_U^{wb}$ and B with $R_D^{bL} Z^{fwb}$, we see that we get nested levels of water reverberations from $[I - R_D^{bL} Z^{fwb}]^{-1}$ modulating the return from depth:

$$\left[I - R_D^{bL} (R_U^{wb} + Z^{fwb}) \right]^{-1} = \left[I - R_D^{bL} Z^{fwb} \right]^{-1}$$

$$+ \left[I - R_D^{bL} Z^{fwb} \right]^{-1} \times R_D^{bL} R_U^{wb} \left[I - R_D^{bL} Z^{fwb} \right]^{-1} + \cdots. \tag{11}$$

As we have noted above, the underside reflection of P waves at the sea surface will be almost complete in the wide angle environment and there will also be efficient wide-angle reflection from the base of the sediments (contained in R_D^{wb}). Similarly Z^{fwb} will be built up from strong reflections from the base of the sediments and the sea-surface, with only modest loss in transmission into and out of the sediments.

Thus irrespective of the detailed nature of the structure of the oceanic lithosphere and mantle beneath, the response at the OBS will be dominated by the set of water reverberations as can be seen in the snapshots shown in Figs 5 and 8. Even in the deep ocean basins the time separation between successive water bounces is only around 5 s for the slowness of *Po* and hardly more than 6 s for the slowness of *So*. The multiple water passes, supplemented by the influence of the sediments, thus form an important means of extending the train of *P*- and *S*-wave energy.

3.2 Influence of lateral variation

The nature of the very strong scattering seen in the seismograms illustrated in Figs 1 and 2 suggests the presence of significant lateral heterogeneity in the oceanic lithosphere. The actual structure is, of course, deterministic, but we can examine the nature of the scattering processes by using 2-D realizations of stochastic heterogeneity.

We employ a von Karman distribution with differing correlation lengths a_x in the horizontal and a_z in the vertical direction. For this stochastic model the probability density distribution in terms of horizontal slowness p and vertical slowness q takes the form

$$P(p, q) = \frac{4\pi\kappa\epsilon^2 a_x a_z}{\left(1 + \omega^2 a_x^2 p^2 + \omega^2 a_z^2 q^2 \right)^{\kappa+1}}, \tag{12}$$

where ϵ is the amplitude of wave speed deviation from the reference. The representation in the spatial domain can then be obtained by Fourier transformation.

We expect the character of heterogeneity to differ between the oceanic crust, the mantle component of the lithosphere and the asthenosphere. We have considered a range of different stochastic structures using the von Karman distribution with differing horizontal and vertical correlation lengths in each of the domains.

Table 2. Heterogeneity parameters in the crust (C), lithosphere (L) and asthenosphere (A) for illustrated models using a von Karman stochastic distribution.

Model class	Zone	Horiz. correl. length a_x (km)	Vertical correl. length a_z (km)	Amplitude ϵ (per cent)	Q_s
D1	C	0.25	5.0	2 per cent	300
	L				2000
	A				450
D2	C	0.25	5.0	2 per cent	300
	L	10.0	0.5	2 per cent	2000
	A				450
D2b	C	0.25	5.0	2 per cent	300
	L	2.24	2.24	2 per cent	2000
	A				450
D2c	C	0.25	5.0	2 per cent	300
	L	∞	0.5	2 per cent	2000
	A				450
D3	C	0.25	5.0	2 per cent	300
	L	10.0	0.5	2 per cent	2000
	A	5.0	1.0	2 per cent	450

We illustrate results for a set of models of stochastic heterogeneity in the crust, lithosphere, and asthenosphere as specified in Table 2. We also vary the lithospheric thickness for the model class D3.

An important feature of typical oceanic crust is the presence of dyke structures. We can incorporate such a structure by imposing stochastic heterogeneity with a dominantly vertical fabric in the crust (model D1). This style of heterogeneity in the 7-km-thick crust has, in fact, very little effect on the wavefield as can be seen by comparing Figs 5(a) and Fig. 7(a). The components of the wavefield spend most of their passage time either in the water and sediments or in the lithospheric mantle, and so the properties of the crust make only a minor effect.

A more significant change is introduced when we include stochastic heterogeneity in the lithospheric mantle in addition to that in the crust. We illustrate a case (model D2) with heterogeneity with a much longer horizontal correlation length than in the vertical direction in Fig. 7(b). Such heterogeneity captures much of the character of observed *Po* and *So* with a much richer and complex coda with little in the way of discrete arrivals beyond 300 km from the source.

Recent work, for example, Kawakatsu *et al.* (2009), suggests that the asthenosphere is also a domain of significant heterogeneity. The inclusion of such heterogeneity with a similar amplitude to that in the lithosphere tends to increase the amplitude of the *Po* and *So* phases slightly (Fig. 7c) because there are now more possibilities for energy to be scattered back into the lithosphere, rather than being lost into the lower wave speed zone of the asthenosphere

The examples in Fig. 7, show how rapidly a complex scattering regime can be established and then sustained for many hundreds of kilometres. We applied a band pass filter with a pass band frequency between 1 and 10 Hz to compare with the examples of observed waveforms (Figs 1 and 2) and each trace is multiplied by $\sqrt{R}$, where R is epicentral distance, to compensate for the geometrical spreading of the 2-D simulation.

Increasing the amplitude of the heterogeneity in the mantle lithosphere has the effect of increasing the level of scattering and tends to push energy later into the coda. The apparent rate of decay of the coda of both *Po* and *So* is therefore reduced.

If we switch the nature of the heterogeneity in the crust to have a horizontal rather than a vertical fabric, then the envelopes of the

Po and *So* tend to become more elongated with less distinct onsets. The vertical dyke scenario is therefore preferable.

It is interesting to compare the apparent attenuation of the wavefield between the base structure and the situation with the introduction of mantle heterogeneity. In the stratified structure the decay rate of *Po* and *So* with distance follow closely the patterns expected for the crustal Q values (Q_p 900; Q_s 450). Whereas, in the quasi-laminate case, the rates of decay are slower and show more variability, but are close to the mantle Q values (Q_p 2000; Q_s 1000). The presence of heterogeneity provides more ways in which energy can propagate through the mantle lithosphere and consequently the significance of mantle paths increases dramatically compared to those in the crust, and so mantle attenuation dominates.

The very significant impact of the presence of stochastic heterogeneity on the seismic wavefield is very clearly seen in Fig. 8 where we show snapshots of the *P* (red) and *S*(green) components of the wavefield at 36, 60 and 96 s after source initiation. Even with a heterogeneous crust with dyke-like structures, the dominant process is water and sediment reverberations with very distinct banded wave fronts. Once heterogeneity is introduced into the oceanic lithospheric mantle the character of the wavefield is changed dramatically. The water reverberations are still present and impose their influence strongly at first, but then scattering takes over and blurs the wave fronts, so that a relatively diffuse wavefield fills the lithosphere. Once established this field is robust and is hardly affected by slow changes in lithospheric properties. In the quasi-laminate case there is also progressive loss of part of the *P* wavefield to *S* that is lost into the mantle below. Even though the crust has lower velocity than the mantle lithosphere, it plays a relatively small role in the transport of seismic energy to large distances.

In Fig. 9, we illustrate the influence of different styles of heterogeneity within the lithsophereic mantle, comparing the case with small-scale isotropic heterogeneity to the model D2 where the horizontal correlation length is much longer than the vertical and the situation where the random heterogeneity varies only with depth. A longer horizontal correlation length tends to concentrate energy towards the front of the *Po/So* phases with a relatively rapid initial decline, but then a long slowly decaying tail. Whereas a shorter
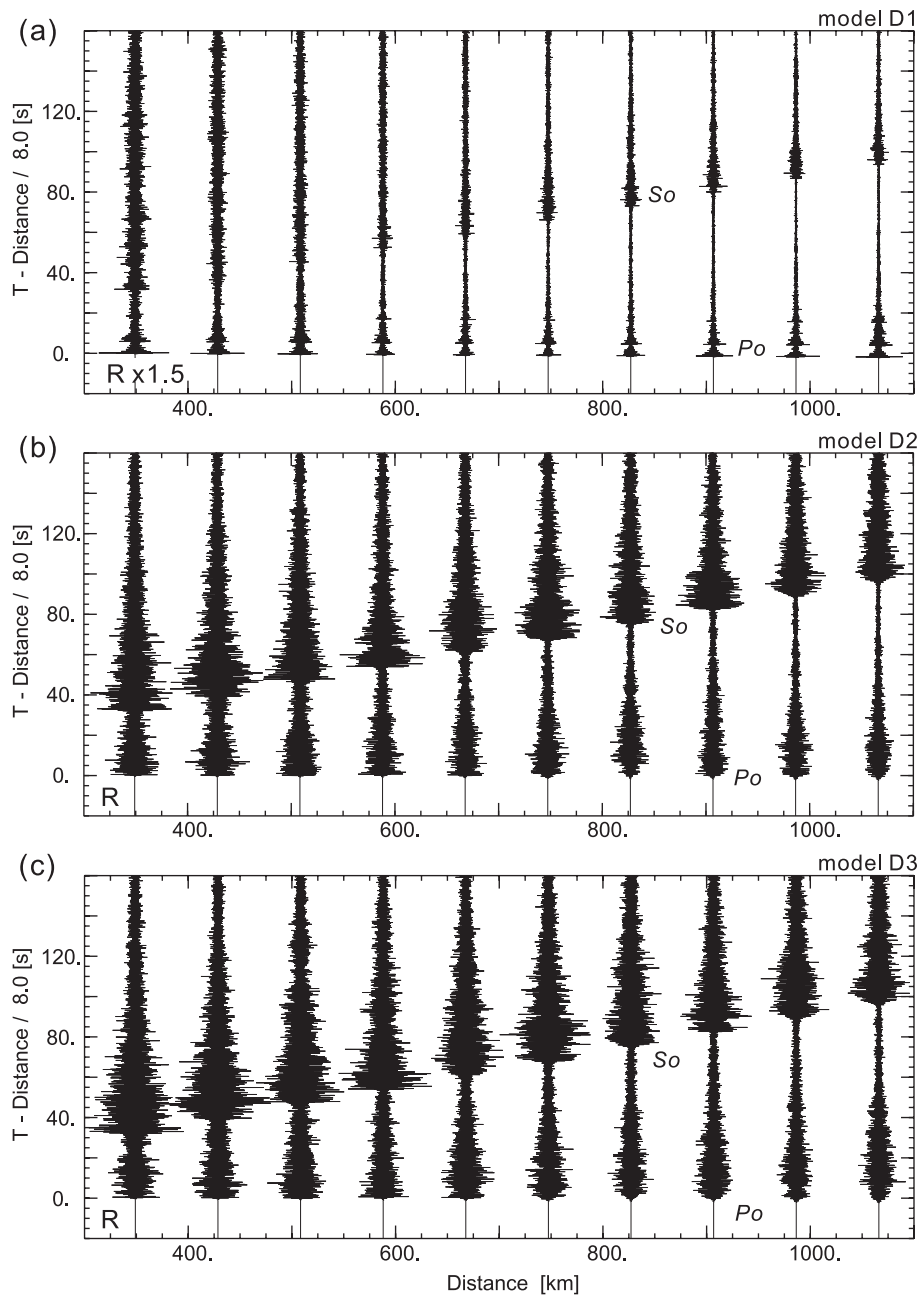
Figure 7. (a) Record section of radial component seismograms for model D1, with a dyke-like structure in the crust (the amplitude is enlarged by a factor of 1.5 to increase visibility), (b) record section of radial component seismograms for model D2, with inclusion also of lithospheric heterogeneity with much longer horizontal correlation length than vertical; (c) with the inclusion of heterogeneity in the asthenosphere below, model D3.

horizontal correlation length tends to produce a longer interval near the front of the wave trains with similar amplitudes. As can be seen from the waveform comparisons in Fig. 9, a stochastic wave speed field with isotropic correlation lengths captures much of the character of the *Po* and *So* though there is some tendency for more bunching of energy towards the onset of the phases, and amplitudes tend to be smaller (Fig. 9a). At the other extreme a 1-D structure with a short vertical correlation length (corresponding to infinite horizontal correlation) also produces relatively realistic waveforms, as suggested by Mallick & Frazer (1990), but displays more distinct sets of arrivals within the wave trains (Fig. 9b). We prefer the intermediate case with quasi-lamination, because this is more consistent

with the situation where the oceanic plate is subducted and strong guiding is observed for high-frequency energy from deep events (Furumura & Kennett 2005, 2008).

Shito *et al.* (2013) undertook a specific comparison of observations and 2-D simulations (to 5 Hz) for a deep focus event beneath Japan observed at an OBS on the Pacific Plate at an epicentral distance of 1000 km. They employed a roughly logarithmic sampling in correlation length (a_x, a_z = 0.5, 1.0, 10, 100 and 1000 km) and reached the conclusion that the correlation lengths in the oceanic lithosphere matched those in the subducting plate, with a horizontal correlation length around 10 km and a vertical correlation length of 0.5 km. This combination successfully explains the envelope shape
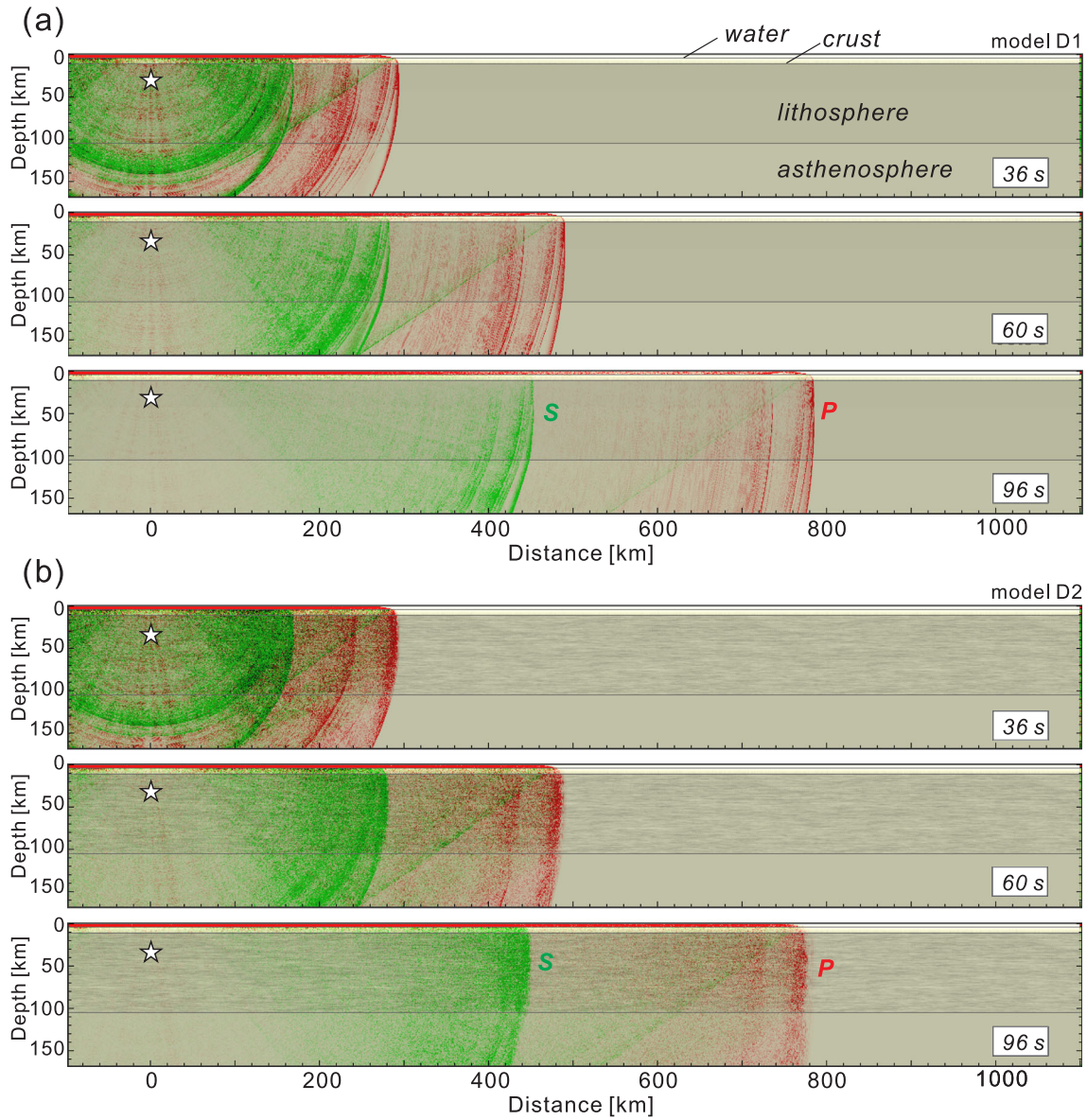
Figure 8. Comparative snapshots of the wavefield for different heterogeneity models: (a) D1 – crustal dyke-like heterogeneity; (b) D2 – crustal and mantle heterogeneity with much longer horizontal correlation length than vertical.

of the *Po* and *So*, and is consistent with the results of our modelling which were taken to higher frequencies.

3.3 Propagation effects from heterogeneity

As displayed in Figs 7–9, the presence of stochastic heterogeneity can rapidly modify the characteristics of the seismic wavefield away from the scenario appropriate for stratification. The heterogeneity regimes of the crustal and mantle portions of the oceanic lithosphere can be quite different, and this will affect the specific characteristics of the propagation process. Nevertheless we will see that the operator representations can provide valuable insight into the behaviour revealed by the numerical simulations for specific realizations of stochastic structures.

We can extend the representation of the seismic wavefield in terms of reflection and transmission operators, we have used in Section 3.1, to show how the action of heterogeneity modifies the

nature of propagation, whilst preserving the dominant effects of the increase in seismic velocities with depth.

We now consider making an explicit split in the structure just below the base of the sediments so that we concentrate on the influence of heterogeneity in the crust and mantle lithosphere (Fig. 6). The energy return from below the base of the sediments R_D^{bL} combines with the near-surface effects in the main reverberation term $[I - R_D^{bL} R_U^{fb}]^{-1}$ (8). We can partition the structure just below the base of the crust at C so that

$$R_D^{bL} = R_D^{bC} + T_U^{bC} \left[I - R_D^{CL} R_U^{bC} \right]^{-1} R_D^{CL} T_D^{bC}, \qquad (13)$$

where R_D^{bC} is the return from the crust and crust–mantle boundary and R_D^{CL} represents return from the mantle. Underside reflection from the crust–mantle boundary appears in R_U^{bC}. Allowing for the main stratification with depth, we can separate the crust and mantle reflection operators into a part associated with the background
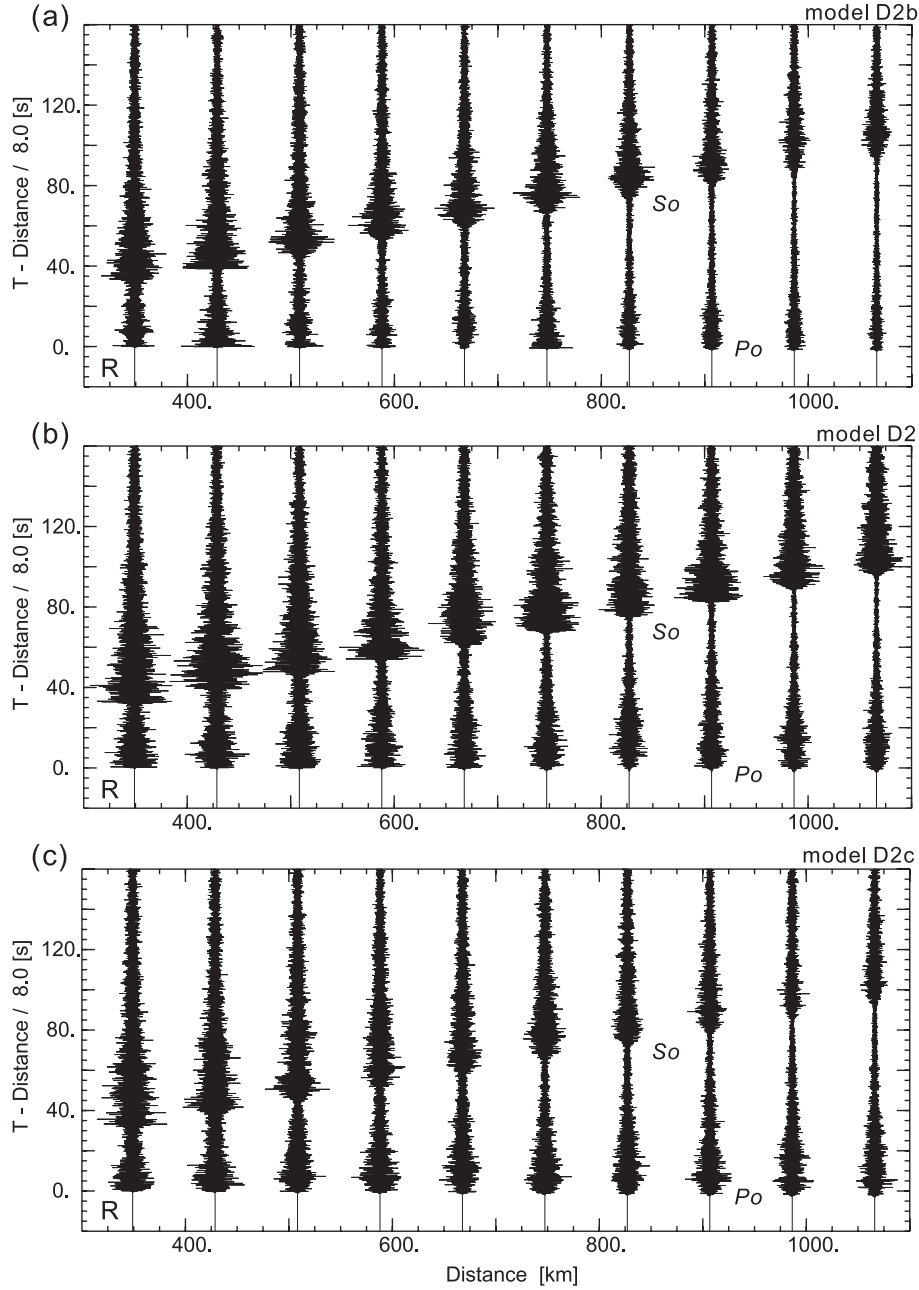
Figure 9. Comparison of wavefield for different classes of lithospheric heterogeneity (a) isotropic correlation lengths ($a_x = a_z = 2.24$ km), (b) model D2 ($a_x = 10$ km, $a_z = 0.5$ km), (c) a 1-D model with the same vertical correlation length ($a_x = \infty$, $a_z = 0.5$ km).

structure and the remainder, including the full effect of lateral variations. Thus we write

$$R_D^{bL} = \left[R_D^{bL}\right]^0 + \check{R}_D^{bL}, \tag{14}$$

where $[R_D^{bL}]^0$ corresponds to the return from the background structure, and $\check{R}_D^{bL}$ is the contribution for lateral heterogeneity. In the wavenumber domain Kennett (1986) has shown that $\check{R}$ induces wavenumber coupling away from an initial wavenumber vector $\mathbf{k}_0$ depending on the wavenumber spectrum of the heterogeneity at the differential vector $\mathbf{k} - \mathbf{k}_0$. It is therefore possible, in principle, to undertake a synthesis in the slowness-frequency domain as for a strictly stratified medium, but now with an allowance for slowness coupling due to the heterogeneity. The computational effort required

is comparable to a direct numerical solution. Nevertheless, the description of the propagation effects is helpful in understanding the influence of lateral heterogeneity.

For a situation with where the horizontal correlation length in a von Karman medium (12) is very much larger than the vertical correlation length ($a_x \gg a_z$), we will get slowness transfer as sketched in Fig. 10. There will be both a spreading of the energy in an initial component into propagation modes with a somewhat different character, and transfer from other scattering interactions. Through multiple interactions with the quasi-stratified structure, the modifications in the vertical slowness will feed back into changing the horizontal slowness characteristics of the wavefield. The span of the slowness interactions is inversely proportional to frequency and the size of the correlation length. Thus as frequency increases,
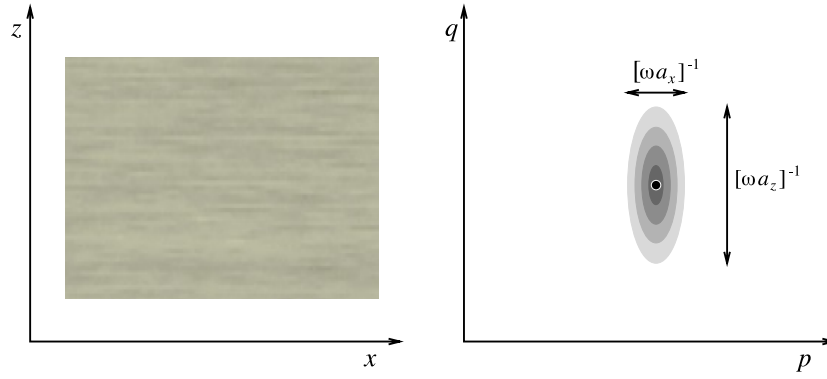
Figure 10. Representation of a stochastic medium with longer horizontal correlation length a_x than vertical a_z, and the corresponding slowness spread from an initial value in slowness space.

shorter scale structures assume greater importance with enhanced efficiency of scattering.

Consider now the full reverberation operator $[I - R_D^{bL} R_U^{fb}]^{-1}$. We can use the partitioned forms (A8), (A9) for the operator inverse developed in the Appendix in two different ways. When heterogeneity is weak, we can emphasize the contributions from the background structure as in Kennett (1986) so that we write

$$\left[I - R_D^{bL} R_U^{fb} \right]^{-1} = \left(I - \left[R_D^{bL} \right]^0 R_U^{fb} \right)^{-1}$$
$$+ \left(I - \left[R_D^{bL} \right]^0 R_U^{fb} \right)^{-1} \times \check{R}_D^{bL} R_U^{fb} \left(I - \left[R_D^{bL} \right]^0 R_U^{fb} \right)^{-1} + \cdots ,$$
(15)

and then each successive interaction with heterogeneity is accompanied by the reverberations in the stratification. This class of representation provides a good description of the character of the arrivals seen for model D1 in Fig. 8(a), where the effect of the crustal dykes is to slightly blur the dominant P and S arrivals that arise from the main stratification.

On the other hand, when multiple scattering is important, as for example, in strong variations about a gentle wave speed gradient, it is more appropriate to write

$$\left[I - R_D^{bL} R_U^{fb} \right]^{-1} = \left\{ I - \check{R}_D^{bL} R_U^{fb} \right\}^{-1}$$
$$+ \left\{ I - \check{R}_D^{bL} R_U^{fb} \right\}^{-1} \times \left[R_D^{bL} \right]^0 R_U^{fb} \left\{ I - \check{R}_D^{bL} R_U^{fb} \right\}^{-1} + \cdots .$$
(16)

Now there will be a strong influence from short wavelengths in the structural variation and slowness coupling will significantly modify the character of the wavefield (Fig. 11). The representation (16) is appropriate to model D2 in which heterogeneity extends through the full mantle lithosphere. The distinct P and S wave fronts seen in Figs 5 and 8(a) are now replaced by a concentration of energy with a distinct coda (Fig. 8b) particularly as the propagation progresses. The coupling between slownesses tends to have the effect of enhancing conversion between near-horizontal P and S waves with similar slowness that travel rather more steeply. The effect is quite evident in the 96 s snapshots of Fig. 8 where the main P wave for model D2, frame (b), sheds a distinct S conversion that is hardly visible for model D1, frame (a). We should recall that in both of the representations (15) and (16), the lithospheric contributions are strongly modulated by the rapid and strong reverberations in the water-sediment zone, as is evident in the snapshots displayed in Fig. 8.
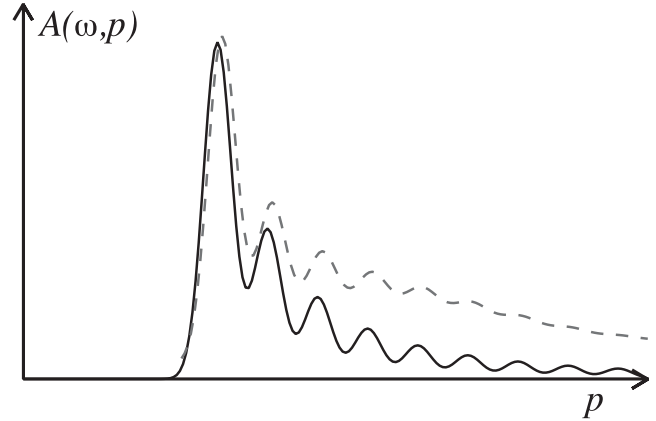

Figure 11. Contribution to a seismic arrival at a distance X in the slowness domain $A(\omega, p)$, comprising a train of distinct successive water reverberations in a stratified medium as shown by the solid line. Slowness coupling due to scattering blurs the separate arrivals, as shown by the dashed curve. The result is elongation of the water reverberations and a much more complex coda to the arrival.

3.4 Influence of lithospheric thickness

The nature of *Po* and *So* depends on the propagation path, as we have seen in Fig. 2. The reduced amplitude of *So* for propagation across the Philippine Sea Plate can be related, in part, to the thinner lithosphere of the younger plate compared with the old thick Pacific Plate. The differences are illustrated in Fig. 12 where we compare waveforms for propagation in old thick lithosphere (110 km depth) and younger thinner lithosphere (30 km depth) for propagation to distances beyond 800 km, with the same values of mantle *Q*. Both *Po* and *So* are very distinct in the thick lithosphere case, but loss into the asthenosphere is more important in the case of thin lithosphere and *So* becomes much less distinct.

In comparison with the observations on the Philippine Sea Plate presented in Fig. 2 the simulations for a thinner lithosphere preserve a somewhat larger *So* phase. The attenuation structure we have used is designed to match the behaviour for the older, colder Pacific Plate and is likely to underestimate the attenuation for *S* waves in the younger, warmer Philippine Sea Plate. It would not take much decrease in Q_S to have a significant suppression of *So* in the 2-D simulations.

Although a thick stochastic waveguide has very robust properties and is little affected by moderate horizontal changes in structure, in the case of a thinner lithosphere the same classes of changes will
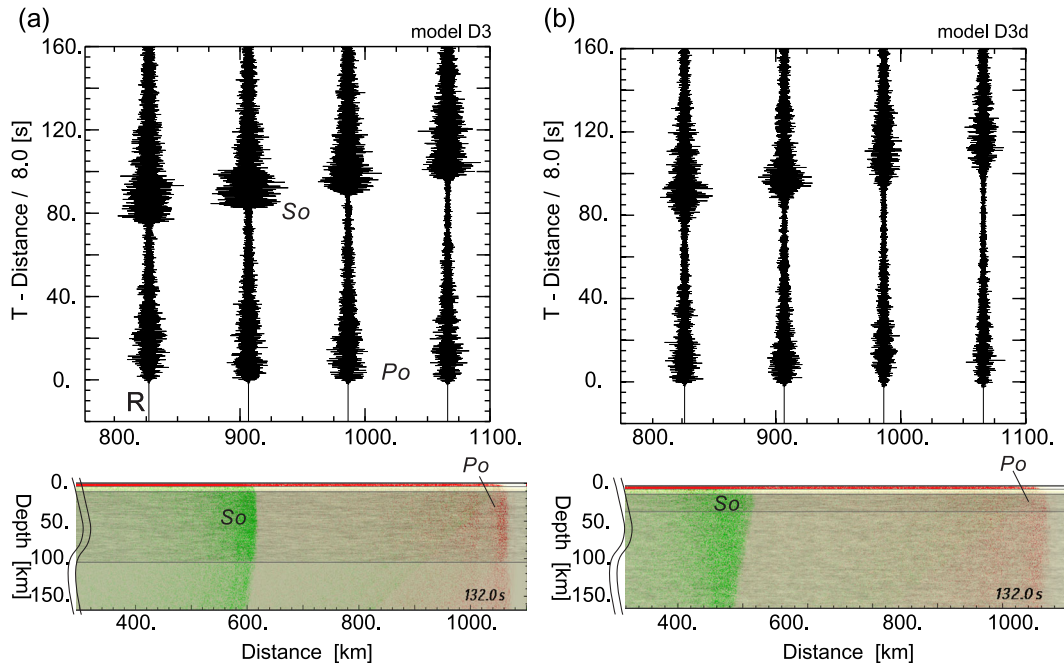
Figure 12. Influence of lithospheric thickness, waveforms for propagation beyond 800 km: (a) old thick lithosphere, (b) young thin lithosphere with heterogeneous asthenosphere.

have much more effect since seismic energy is more easily lost. We will explore this issue further in the companion paper (Kennett *et al.* 2013, in preparation) where we look at the geographic patterns of *Po* and *So* propagation and their relations to the character of the lithosphere.

4 DISCUSSION AND CONCLUSIONS

In Fig. 13, we present a comparison of the observations for paths across the Pacific and Philippine Sea plates from Fig. 2 and the results of the 2-D numerical simulations at comparable distances. We compare the radial component seismograms for a variety of

models with different patterns of heterogeneity, extracting the traces for epicentral distances close to 960 km from Figs 5 to 12. In all cases the records bear the strong imprint of reverberations in the water and shallow sediment structure.

As noted above, a simple stratified structure (Fig. 13c) produces a long duration record composed of a sequence of distinct pulse-like arrivals. The inclusion of dyke-like structures (Fig. 13d) in the crust is preferable to horizontally elongated features, and is more consistent with expected structures, however, the heterogeneity in the thin crust yields little effect on the wavefield.

The dominant influence on the character of the seismic records comes from the heterogeneity in the mantle lithosphere because the passage time through the crust is short compared to the total
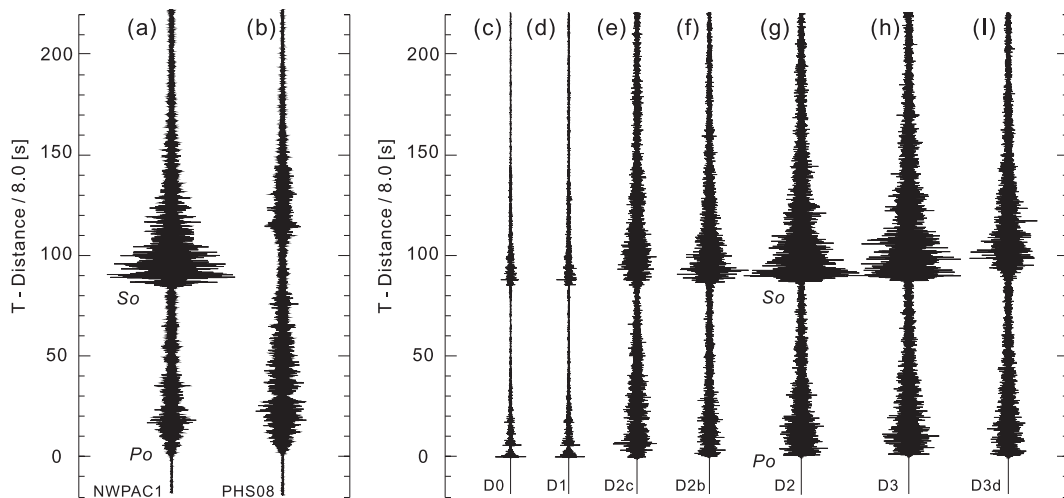
Figure 13. Comparison of observed radial component seismograms for epicentral distance close to 1000 km: (a) at NWPAC traversing Pacific Plate, (b) at PHS08 traversing the Philippine Sea Plate, with synthetic seismograms at 960 km: (c) simulation for horizontally stratified base model, (d) model D1 with just crustal dykes, (e) model D2c with 1-D random heterogeneity in the lithospheric mantle, (f) model D2b with isotropic heterogeneity in the lithospheric mantle, (g) model D2 with quasi-laminate heterogeneity in the lithospheric mantle, (h) model D3 incorporating asthenospheric heterogeneity with that of model D2, (i) model D3d with thinner lithosphere (30 km thick).

propagation time. The addition of 1-D random heterogeneity in the lithosphere (Fig. 13e) and 2-D random heterogeneity with a isotropic correlations, that is, the same correlation distance in the horizontal and vertical directions (Fig. 13f) modifies the wavefield towards the appearance of the observations, but does not give a strong *So* arrival.

The character of the observations in the Pacific Plate is best matched in our 2-D simulations with a situation in which the heterogeneity has much longer horizontal than vertical correlation lengths (Fig. 13g). There is only a modest increase in complexity when heterogeneity is included in the asthenosphere as well (Fig. 13h).

The thickness of the lithosphere plays an important role in shaping the details of the seismogram, and will also interact strongly with attenuation structure. Thick lithosphere with quasi-laminate heterogeneity (Fig. 13h) provides a good representation of the character of the observations for passage through the Pacific Plate (Fig. 13a). Whereas the introduction of a much thinner lithosphere as in Fig. 13(i) generates seismograms with a character more comparable to that seen for Philippine Sea Plate paths (Fig. 13b).

4.1 Nature of heterogeneity

In this work we have concentrated on the general properties of the *Po* and *So* phases, recognizing that there can be significant differences in the character of the seismograms as seen on different paths. The simulations have been undertaken in specific realizations of a 2-D stochastic model, whereas the oceanic lithosphere is undoubtedly heterogeneous in 3-D. The complex seismograms on the tangential component in the -wave interval (Fig. 2) provide clear evidence for such 3-D seismic scattering effects.

In consequence we are able to suggest a class of heterogeneity that is compatible with the broad range of observations, with much longer horizontal correlation length than in the vertical direction. However, we do not have very strong constraints on the horizontal correlation length of the lithospheric heterogeneity, though it appears that it is likely to be around 10–20 km (as was also suggested by Shito *et al.* 2013). This result is consistent with our earlier studies of heterogeneity in the subduction zone environment for the Pacific Plate (Furumura & Kennett 2005).

The class of heterogeneity which best represents the character of the *Po* and *So* in our 2-D simulations requires moderate fluctuations in seismic wave speed away from the background structure that would not be revealed by analysis with longer period waves. The levels of heterogeneity are not difficult to produce in either a peridotic or eclogitic scenario (*cf.* Mallick & Frazer 1990) for the composition of the lithosphere, by local variations in processes of accretion of the mantle component of the lithosphere, for example, by underplating, which would also be compatible with the much longer horizontal correlation length than in the vertical direction.

As we have seen dyke-like structures in the crust with a dominant vertical orientation do not disrupt the wavefield, because of the rapid passage through the thin oceanic crust. The constant reinforcement of the field through the reverberations in the water column and sediments will also tend to maintain the character of the wavefield once it is established. With horizontal correlation lengths in the mantle lithosphere of several wavelengths, the structure will appear locally as approximately stratified with an enhancement of forward scattering from low angle reflections.

The multiply scattered waves propagating through the oceanic lithosphere in the form of *Po* and *So* and their coda are restricted to a limited range of slownesses with wave trains elongated by near

surface reverberation and 'whispering gallery' effects in the lithosphere. The net result is that a relatively diffuse wavefield pervades the lithosphere, channelled forwards by the quasi-laminar nature of the heterogeneity. This wavefield is quite resilient, and little affected by variations in lithospheric thickness unless they occur very rapidly. At 10 Hz the *P* wavelength is just over a kilometre and the *S* wavelength around 0.6 km. Thus, a change occurring over a 20–30 km distance span would represent many wavelengths of the higher frequency waves. The limited impact of such a change found in numerical simulations of *Po* and *So* reflects the continual wave interactions in the complex structure so that both modest thickening and thinning of the stochastic waveguide in the lithosphere can be accommodated without major distortion of the propagation characteristics.

Our preferred class of lithosphere heterogeneity has a strong resemblance to that proposed by Kawakatsu *et al.* (2009) for asthenospheric structure beneath the Philippine Sea Plate. In their 'mille-feuille' model thin pods of melt are surrounded by solid and the horizontal dimensions of the pods are much longer than the vertical. The wave speed contrasts induced by the presence of melt are large. However, if the temperature were to drop sufficiently for the melt to freeze, the contrasts would be dramatically reduced, and we would have a scenario very like that we have proposed for the lithosphere. Thus this class of heterogeneous structure with quasi-laminar structure would be compatible with lithospheric growth by underplating from below.

Although all of the structures we have been considering are built from isotropic materials, the quasi-laminated structure will appear anisotropic when probed by longer wavelengths with, for example, faster *S*-wave propagation in the horizontal direction than vertical. As a result of wavefield averaging, the material will appear transversely isotropic, with a level of polarization anisotropy around 1.5 per cent for our preferred models in which the local wave speeds vary by up to 4 per cent in rapid vertical succession. Thus the heterogeneous lithospheric structure will contribute to the recognized anisotropic structure in the Pacific Plate (e.g. Ekström 2011).

4.2 3-D heterogeneity

Our modelling has concentrated on vertical sections through the lithosphere, and so cannot say anything about the pattern of heterogeneity in the horizontal plane. The heterogeneity structure in the oceanic lithosphere will be carried into the downgoing plate through the process of subduction, and will influence the propagation of seismic waves in the plate from deep earthquakes. Furumura & Kennett (2005) were able to demonstrate the way in which heterogeneity with a longer correlation length along the subducting plate compared with the cross-plate direction was able to sustain high-frequency energy from even the deepest events. Yet, in their 3-D simulations, it was not possible to match the extent of guided energy along the plate. For example, a 360 km deep event near the Kii peninsula, on the southern coast of central Japan, produced noticeable ground motion all along the eastern seaboard of Honshu from Tokyo to Tohoku and into Hokkaido. This significant ground motion is observed over a distance of more than 1000 km from the source. The 3-D modelling of a heterogeneous plate with equal correlation lengths in the plane of subduction certainly produced extension of the areas of significant intensity towards the north, but by no means as far as in the observations (see fig 1b in Furumura & Kennett 2005).

The 3-D model used by Furumura & Kennett (2005) employed heterogeneity with an equal correlation length along and down the subducting plate ($a_x = a_y = 10$ km), with a much shorter correlation length across the thickness of the plate ($a_z = 0.5$ km). A modest elongation of the planform of the heterogeneity in the plate, with the larger correlation length in the direction of the magnetic lineations in the northwestern Pacific, would be oriented to enhance ducting of energy towards the north, and thereby help to reconcile the 3-D simulations with the observations. There will be some enhancement of the guiding of high-frequency waves in the direction of maximum horizontal correlation length to reinforce the effects of the quasi-laminar structure across the thickness of the plate.

ACKNOWLEDGEMENTS

REFERENCES

Brandsdóttir, B. & Menke, W., 1988. Measurements of coda buildup and decay rates of Western Pacific P, Po and So phases and their relevance to lithospheric scattering, *J. geophys. Res.,* **93,** 10 541–10 559.

Ekström, G., 2011. A global model of Love and Rayleigh surface wave dispersion and anisotropy 25–250 s, *Geophys. J. Int.,* **187,** 1668–1686.

Fuchs, K. & Schulz, K., 1976. Tunneling of low-frequency waves through the subcrustal lithosphere, *J. Geophys.,* **42,** 175–190.

Furumura, T. & Chen, L., 2004. Large scale parallel simulation and visualization of 3-D seismic wavefield using the Earth Simulator, *Comput. Mode. Eng. Sci.,* **6,** 153–168.

Furumura, T. & Kennett, B.L.N., 2005. Subduction zone guided waves and the heterogeneity structure of the subducted plate - intensity anomalies in northern Japan, *J. geophys. Res.,* **110,** B10302, doi:10.129/2004JB003486.

Furumura, T. & Kennett, B.L.N., 2008. A scattering waveguide in the heterogeneous subducting plate, in *Scattering of Short-Period Seismic Waves in Earth Heterogeneity,* Advances in Geophysics, Vol. 50, Chap. 7, pp. 195–217, eds Sato, H. & Fehler, M., Elsevier.

Gettrust, J. & Frazer, L.N., 1981. A computer model study of the propagation of the long range Pn phase, *Geophys. Res. Lett.,* **8,** 749–752.

Hestholm, S., 1999. Three-dimensional finite difference viscoelastic wave modelling including surface topography, *Geophys. J. Int.,* **139,** 852–878.

Jackson, I., 2007. 2.17: properties of rocks and minerals? Physical origins of anelasticity and attenuation in rock, *Treatise on Geophysics,* Vol. 2: Mineral Physics, pp. 493–525, Elsevier.

Kawakatsu, H., Kumar, P., Takei, Y., Shinohara, M., Kanazawa, T., Araki, E. & Suyehiro, K., 2009. Seismic evidence for sharp lithosphere-asthenosphere boundaries of oceanic plates, *Science,* **324,** 499–502.

Kennett, B.L.N., 1984. Reflection operators for elastic waves II—composite regions and source problems, *Wave Motion,* **6,** 419–429.

Kennett, B.L.N., 1986. Wavenumber and wavetype coupling in laterally heterogeneous media, *Geophys. J. R. astr. Soc.,* **87,** 313–331.

Kennett, B.L.N., 2001. *The Seismic Wavefield I: Introduction and Theoretical Development,* Cambridge University Press.

Kennett, B.L.N. & Furumura, T., 2008. Stochastic waveguide in the Lithosphere: Indonesian subduction zone to Australian Craton, *Geophys. J. Int.,* **172,** 363–382.

Maeda, T. & Furumura, T., 2013. FDM Simulation of seismic waves ocean acoustic waves and tsunamis based on tsunami-coupled equations of motion , *Pure appl. Geophys.,* **170,** 109–127.

Mallick, S. & Frazer, L.N., 1990. *Po/So* synthetics for a variety of oceanic models and their implications for the structure of the oceanic lithosphere, *Geophys. J. Int.,* **100,** 235–253.

Marcinkovich, C. & Olsen, K., 2003. On the implementation of perfectly matched layers in a three-dimensional fourth-order velocity-stress finite difference scheme, *J. geophys. Res.,* **108**(B5), 2276, doi:10.1029/2002JB002235.

Menke, W.H. & Richards, P.G., 1980. Crust-mantle whispering gallery phases: a deterministic model of teleseismic *Pn* wave propagation, *J. geophys. Res.,* **85,** 5416–5422.

Moczo, P., Robertsson, J.O.A. & Einsterd, L., 2007. The finite- difference time-domain method for modeling of seismic wave propagation, in *Advances in Wave Propagation in Heterogeneous Earth,* Advances in Geophysics, Vol. 48, eds, Wu, R.-S. & Maupin, V., Elsevier, doi:10.1016/S0065-2687(06)48008-0.

Okamoto, T. & Takenaka, H., 2005. Fluid-solid boundary implementation in the velocity-stress finite-difference method, *Zisin 2,* **57,** 355–364 [in Japanese].

Shiobara, H., Kanazawa, T. & Fukao, Y., 2005. Revealing the Earth's interior by using mobile broadband ocean bottom seismometers, *Chikyu Mon.,* **51,** 181–187 [in Japanese].

Shito, A., Suetsugu, D., Furumura, T., Sugioka, H. & Ito, A., 2013. Small-scale heterogeneities in the oceanic lithosphere inferred from guided waves, *Geophys. Res. Lett.,* **40,** doi:10.1002/grl.50330.

Sereno, T.J. & Orcutt, J.A., 1985. Synthesis of realistic oceanic P$_n$ wavetrains, *J. geophys. Res.,* **90,** 12 755–12 776.

Sereno, T.J. & Orcutt, J.A., 1987. Synthetic P$_n$ and S$_n$ phases and the frequency dependence of Q of oceanic lithosphere, *J. geophys. Res.,* **92,** 3541–3566.

Takemura, S., Furumura, T. & Saito, T., 2009. Distorion of the apparent radiation pattern in the High-frequency wavefield: Tottori-ken Seibu, Japan, Earthquake of 2000, *Geophys. J. Int.,* **178,** 950–961.

Walker, D.A. & Sutton, G.H., 1971. Oceanic mantle phases recorded on hydrophones in the North Western Pacific at distances between 9 and 40, *Bull. seism. Soc. Am.,* **61,** 65–78.

Walker, D.A., McCreery, C.S. & Sutton, G.H., 1983. Spectral characteristics of high frequency *Pn*, Sn phases in the Western Pacific, *J. geophys. Res.,* **88,** 4289–4298.

APPENDIX: EXPANSION OF REVERBERATION OPERATORS

In many circumstances we encounter a reverberation operator of the form $[I - A - B]^{-1}$, where I is the identity and A, B correspond to different combinations of reflection elements associated with separate classes of wave propagation processes.

The general operator relation

$$[I - X]^{-1} = I + X[I - X]^{-1}, \tag{A1}$$

can readily be verified by post-multiplication by $[I - X]$. With progressive application of (A1), a reverberation operator can be represented as a power series in X.

$$[I - X]^{-1} = I + X + X.X + X.X.X + \cdots. \tag{A2}$$

When the operator combination X is given by a sum $X = A + B$, we would like to place emphasis on either A or B, and seek representations in which partial reverberations dominate. Suppose we write

$$[I - A - B]^{-1} = [I - B]^{-1}Y \tag{A3}$$

and seek to find the appropriate operator Y. Eliminating the two operator inverses by multiplication, we obtain

$$[I - B] = Y[I - A - B], \tag{A4}$$

so that

$$I = Y - Y.A[I - B]^{-1}, \tag{A5}$$

and thus

$$[I - A - B]^{-1} = [I - B]^{-1}[I - A[I - B]^{-1}]^{-1}. \tag{A6}$$

An alternative form obtained in a similar way is

$$[I - A - B]^{-1} = [I - B]^{-1}[I + A[I - A - B]^{-1}]. \tag{A7}$$

In each case is we apply the reverberation operator relation recursively we obtain,

$$[I - A - B]^{-1} = [I - B]^{-1} + [I - B]^{-1}A[I - B]^{-1} + [I - B]^{-1}$$
$$\times A[I - B]^{-1}A[I - B]^{-1} + \cdots, \tag{A8}$$

so that successive interactions with process A are accompanied by the partial reverberation terms $[I - B]^{-1}$.

Since the selection of the parts A and B is arbitrary there is an analogous development to (A8) in terms of the partial reverberations $[I - A]^{-1}$

$$[I - A - B]^{-1} = [I - A]^{-1} + [I - A]^{-1}B[I - A]^{-1} + [I - A]^{-1}$$
$$\times B[I - A]^{-1}B[I - A]^{-1} + \cdots. \tag{A9}$$

As can readily be seen, the expressions (A8) and (A9) place very different emphasis on the components of the wave propagation processes. The particular form to be chosen for the reverberation operator and, indeed, the partitioning of the reflection combinations into the terms A and B will depend on the nature of the situation.